ACS Photonics

Article

pubs.acs.org/journal/apchd5

A Local Superlens

Susanne C. Kehr,*[,†] Raymond G. P. McQuaid,[‡] Lisa Ortmann,[†] Thomas Kämpfe,[†] Frederik Kuschewski,[†] Denny Lang,[†,§] Jonathan Döring,[†] J. Marty Gregg,[‡] and Lukas M. Eng[†]

[†]Institute of Applied Physics, Technische Universität Dresden, 01062 Dresden, Germany

[‡]Centre for Nanostructured Media, School of Maths and Physics, Queen's University Belfast, Belfast BT71NN, United Kingdom

[§]Helmholtz-Zentrum Dresden-Rossendorf, Institute of Ion Beam Physics and Materials Research, Bautzner Landstraße 400, 01328 Dresden, Germany

Supporting Information

ABSTRACT: Superlenses enable near-field imaging beyond the optical diffraction limit. However, their widespread implementation in optical imaging technology so far has been limited by large-scale fabrication, fixed lens position, and specific object materials. Here we demonstrate that a dielectric lamella of subwavelength size in all three spatial dimensions behaves as a compact superlens that operates at infrared wavelengths and can be positioned to image any local microscopic area of interest on the sample. In particular, the lamella superlens may be placed in contact with any type of object and therefore enables examination of hard-to-scan samples, for example, with high topography or in liquids, without altering the specimen design. This lamella-based local superlens design is directly applicable to subwavelength light-based technology, such as integrated optics.

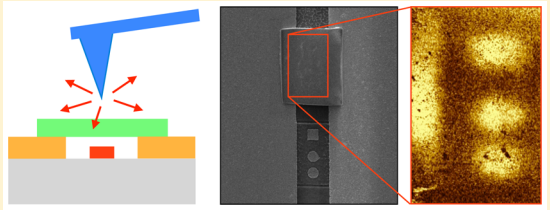

KEYWORDS: *superlens, subwavelength imaging, near-field microscopy, barium titanate, mid-infrared, free-electron laser*

Standard optical microscopy reaches a typical diffraction-limited resolution on the order of half the wavelength λ. However, the need for imaging on the nanoscopic and molecular scale led to the development of optical techniques that beat this limit, such as super-resolved fluorescence microscopy (Nobel Prize in Chemistry 2014)[1−3] and scanning near-field optical microscopy (SNOM).[4,5] The latter reaches a wavelength-independent resolution of typically 10 nm and has witnessed particular interest at infrared (IR) wavelengths for molecular fingerprinting,[6,7] phonon spectroscopy in crystals,[8−10] and inter- or intraband transitions in quantum dot structures.[11]

On the other hand, the observation of nanoscopic optical phenomena is accompanied by a novel light-based technology on the subwavelength scale such as integrated optical circuits, optical computing, and medical applications.[12] For example, near-field superlenses are known to reconstruct the evanescent waves of the objects in their image planes within the near-field regime of the lenses.[13,14] Such a superlens may be realized by a planar slab of material, that is excited close to polaritonic resonances, for example, at the phonon resonances in dielectrics,[15−17] as well as at the plasmon resonances for metals,[18] semiconductors,[19] or graphene.[20,21] The imaging capabilities of such a lens are not limited by diffraction; however, the optical resolution and the signal contrast are reduced by material absorption and interface roughness.[15,16,19,22] Perovskite oxides are particularly suited for low-loss superlensing at mid-IR wavelengths.[16,17] Nevertheless, to date, those lenses are restricted in applicability to accurate spacer-layer matching, to specific object materials and by unwanted topographic features.[15−17] Furthermore, these fixed-position superlenses were fabricated by thin-film growth and so far were designed solely in a laterally large-scale fashion.[16,17,19]

In this paper, we present a superlens that overcomes all of these limitations. This lens is based on a subwavelength-sized lamella carved out of a bulk barium titanate ($BaTiO_3$, BTO) single crystal (sc) by means of focused ion beam (FIB). This BTO slab can be placed down on any desired area of interest using micromanipulation, resulting in a highly positionable, local-area superlens. The topography of such a lamella superlens is perfectly flat, showing a typical RMS roughness of 0.5−5 nm.[23] As the lamella is obtained from a bulk sc, the sample crystallographic structure and lamella's dielectric and optical properties are excellently known. Moreover, the lamella lens may be easily suspended over the structure of interest, hence facing no limits in application to specific objects or object materials. Since it is freestanding in air in our current design, there is no need for finding a specific matching material as the spacer layers.

The simple design of the lens and particularly its ultrasmall dimensions (being $<\lambda$ in all three spatial directions) enable integration into compact optics such as lab-on-chip structures without dramatic changes to the overall sample geometry. Especially, for hard-to-scan-systems in liquids or with significant topographical variation, remote optical sensing via near-field superlensing is directly enabled. Here, BTO is utilized as an exemplary representative of perovskite oxides showing well-

Received: July 3, 2015
Published: December 7, 2015

DOI: 10.1021/acsphotonics.5b00365
ACS Photonics 2016, 3, 20−26

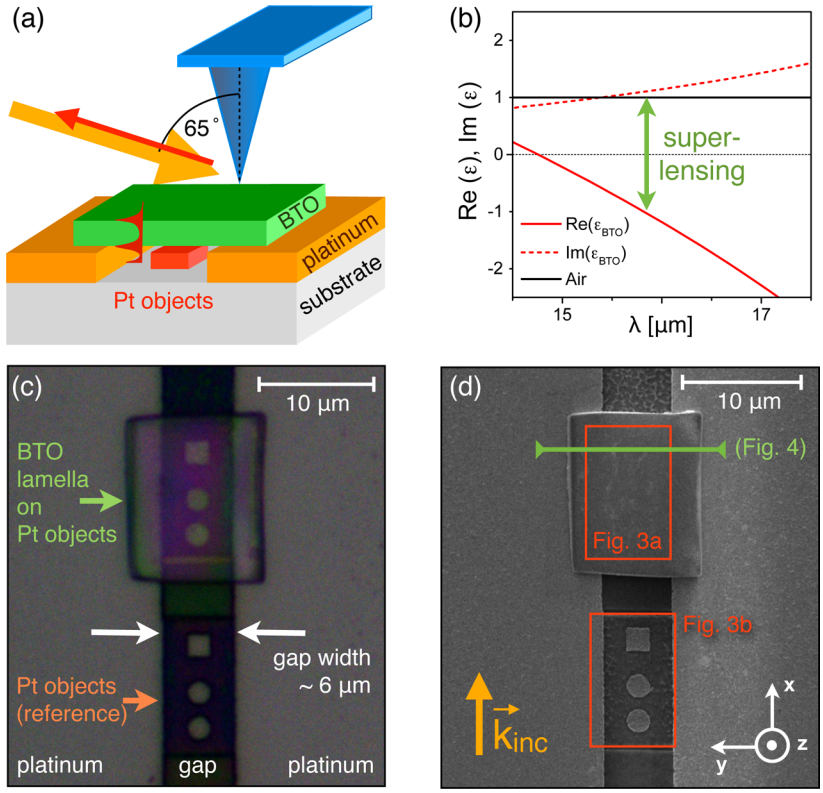

Figure 1. Sample structure. (a) Sketch of s-SNOM geometry and sample structure, including the SNOM probe (blue) and the BTO lamella (green), that has been placed over a 6 μm wide trench within a Pt film (orange) on a silicon substrate (gray). Within the gap, Pt objects (red) are located next to the lamella for reference as well as underneath the lamella with a gap of ~100 nm between objects and lamella. (b) Real parts of the permittivities of BTO[24] and of the surrounding (air) that result in superlensing around λ = 16.5 μm. (c) Optical microscopy image of the sample showing the sample structure and, in particular, the position of the objects underneath the lamella (note that BTO is transparent at visible wavelengths). (d) Scanning electron microscopy map exhibiting finer details of the structure within the gap. Here, we marked the areas of the near-field examination (red areas and green line), as presented in Figures 3a,b and 4, as well as the direction of the incident **k**-vector in the sample plane and the coordinate system used in Figures 2–4.

defined phonon modes for superlens excitation in the mid-IR[16,17] and moreover exhibiting strong photorefractive and electro-optic responses that enable for further extensions of superlensing toward optical phase conjugation[24] and electro-optic tuning,[16,17] respectively. However, the proposed design of the local superlens is not limited to BTO, but can be applied to any superlensing material that can be fabricated into a subwavelength size, hence, covering a wavelength regime from UV and visible light for metals, near-infrared for doped semiconductors, to the mid-IR for polar dielectrics.[22]

RESULTS AND DISCUSSION

Lamella Superlens. The lamella superlens introduced here measures 13.5 μm × 10.5 μm × 400 nm and with that is subwavelength in size for all three spatial directions at the superlensing wavelength of λ_{SL} = 16.5 μm (Figure 1a,b). It consists of a planar slab of single crystalline BTO balancing across the objects of interest that are located within a ~0.3 μm deep trench in a platinized silicon substrate. Each set of subwavelength-sized platinum (Pt) objects consists of a 2 μm × 2 μm square and two 2 μm diameter circles with a height of ~200 nm (see Figure 1c,d). For details on the sample preparation, including FIB fabrication of lamella and objects, see Methods.

The optical microscope image in Figure 1c shows the sample structure with the platinized silicon substrate, trench, lamella, and structured objects within the gap. Note that we may even see the objects to be imaged that are located underneath the lamella, since BTO is transparent at visible wavelengths. The duplicate structure next to the lamella shows the same Pt objects and is used as a reference. In a scanning electron microscopy (SEM) image of the structure (Figure 1d), even finer details are discerned, such as steps in the gap due to the structuring process. We also highlighted in this figure the direction of the incident **k**-vector, as well as all the areas where the near-field investigations in Figures 3a,b and 4 were performed.

Working Principle of Superlensing. BTO shows a phonon resonance[25] around 20 μm resulting in superlensing close to λ_{SL} = 16.5 μm when considered free-standing in air. Here, the superlensing condition[13,14] $\mathrm{Re}(\varepsilon_{SL}) = -\mathrm{Re}(\varepsilon_{air}) = -1$ is met as indicated in Figure 1b. Origin of this effect is a coupled mode of polaritons at both interfaces of the BTO lamella that transfers the electric fields from the object side to the image side of the lens. Figure 2a,b shows numerical simulations (via COMSOL 5.0) of the electric field distribution originating from two point dipoles for selected wavelengths. At λ = 14 μm, $\mathrm{Re}(\varepsilon_{BTO}) \approx 1$ and the dipole fields are unaffected (except for slight absorption), whereas for λ = 18 μm nonlocalized polaritons at the BTO interfaces are excited. Only around the superlensing wavelength of λ = 16.5 μm, an image is formed on the opposite side of the slab within the near-field regime of the lens.

DOI: 10.1021/acsphotonics.5b00365
ACS Photonics 2016, 3, 20–26

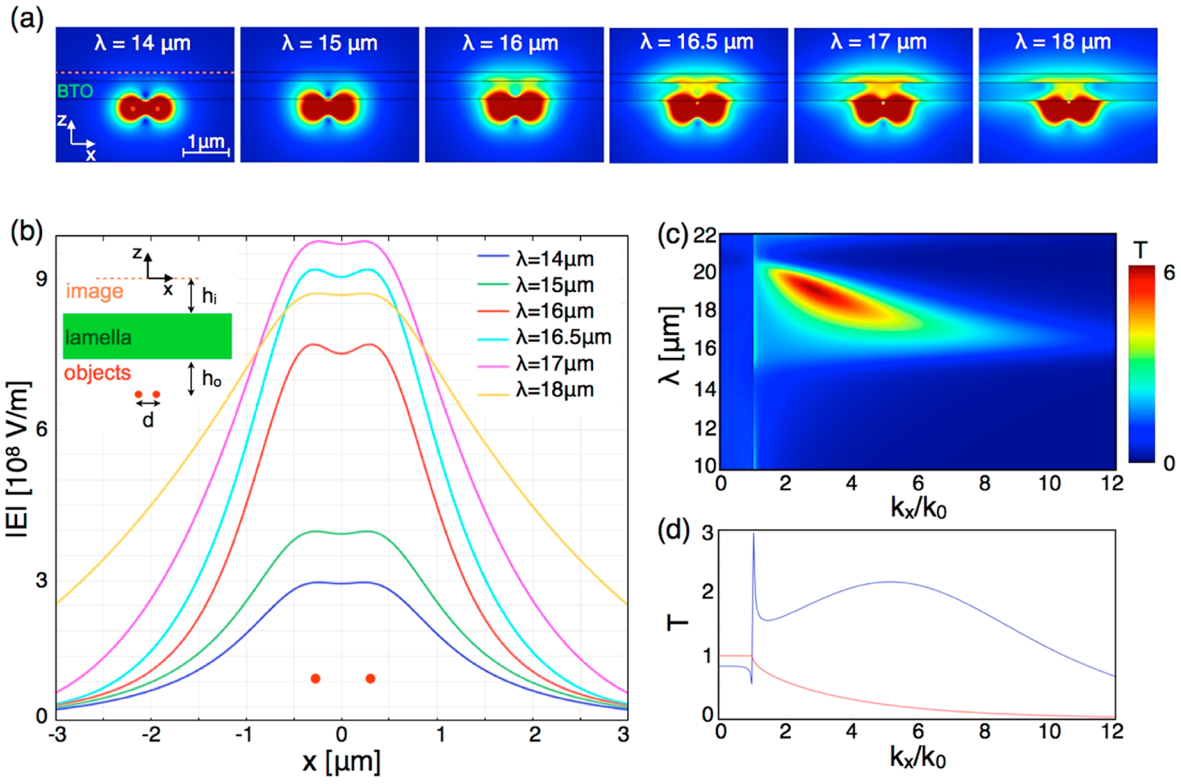

Figure 2. Theoretical description of the 400 nm thick BTO superlens. (a) Electric field distribution of two point dipoles (d = 0.55 μm, h_0 = 200 nm). Depending on the wavelength, the slab is passive (λ = 14 μm, Re(ε_{BTO}) = ε_{Air} = 1), creates a superlensed image (λ = 16−17 μm), or excites nonlocalized polariton modes at the BTO interfaces (λ = 18 μm). (b) Electric field along the image line at h_i = 200 nm for selected wavelengths. For superlensing around λ_{SL} = 16.5 μm, the two point dipoles are clearly separated corresponding to a resolution of λ/30. (c) The isothermal contour of transfer function T is plotted versus wavelength λ and tangential wave vector k_x. At the superlensing wavelength, T shows an extended tail toward large k_x, according to the enhancement of high k_x-components that form the superlens image. (d) Transfer functions of the superlens (blue) and of air reference (red) are displayed versus k_x for λ = 16.5 μm. The superlens enhances the evanescent waves over a wide range of k_x up to 12 k_0.

As structure sizes much smaller than the wavelength are directly attributed to large tangential wave vectors $\mathbf{k}_x$, their reconstruction in an image is only possible when the corresponding $\mathbf{k}_x$ are supported and transferred by the lens. Analytically, the superlensing effect can be described by the transfer function $T = |t|^2$ being the square of ratio between the electric field transmitted through the superlens and the incident field.[26,27] In the isothermal contour plot of the transfer function (Figure 2c) superlensing appears at λ = 16.5 μm as an elongated tail of T up to large $\mathbf{k}_x$. In Figure 2d, the transfer function for this wavelength is plotted as a function of $\mathbf{k}_x$, revealing an enhanced transfer of TM waves to the object interface of the lamella even for a tangential wave vector $\mathbf{k}_x$ up to 12 k_0. For additional theoretical considerations concerning the role of lateral superlens dimensions, see Supporting Information, Figure S1.

Near-Field Characterization. The lamella sample was inspected by our scattering scanning near-field optical microscope (s-SNOM) that is combined with the tunable free-electron laser (FEL) FELBE at the Helmholtz-Zentrum Dresden-Rossendorf.[9,10,16,17] The FEL covers the broad range from 4 to 250 μm in wavelength, hence, excellently matching the needs for resonant BTO lamella excitation around λ_{SL} = 16.5 μm. In order to separate near- and far-field signals, the directly backscattered signal is demodulated at multiples n of the cantilever oscillation frequency Ω, resulting in the higher-harmonic near-field signals $NF_{n\Omega}$.[8,28,29] The presented $NF_{n\Omega}$ are raw data that were normalized to the in situ monitored incident power densities. Details on the s-SNOM, including the basis noncontact atomic force microscope (nc-AFM), and the optical setup are given in Methods.

Near-field signatures have been recorded from the BTO-lamella and the reference structure. In the following, we present scans on specific areas of the sample revealing the subdiffraction limited resolution of the superlens (Figure 3). Moreover, cross sections along a line as marked in Figure 1d (Figure 4) prove the evanescent character of the signal. Finally, the spectral responses on different sample areas are discussed (Figure 5).

Subdiffraction-Limited Resolution. The near-field scans of the lamella superlens at λ = 16.5 μm are displayed in Figure 3a for the different demodulations at higher harmonics $n\Omega$ (with n = 2, 3, and 4). The optical image of the dot structure underneath the lamella is clearly reconstructed at the top surface of the lamella showing decreasing far-field contributions with increasing harmonic order n. The two circular dots of 2 μm diameter and 1 μm separation are clearly distinguishable and prove subdiffraction-limited resolution of at least λ/16. In Figure 3b, the corresponding near-field signals on the reference structure are displayed using the same color scale. Note that scanning these structures within the gap is challenging due to the comparably large sample topography of ~300 nm resulting, for example, in an asymmetric appearance of the objects. Compared to the original signal on the reference structure, the superlensed image appears blurred. However, due to the resonant excitation of the lamella the signal strength of the reconstructed image on the superlens is enhanced, and the

DOI: 10.1021/acsphotonics.5b00365
ACS Photonics 2016, 3, 20−26

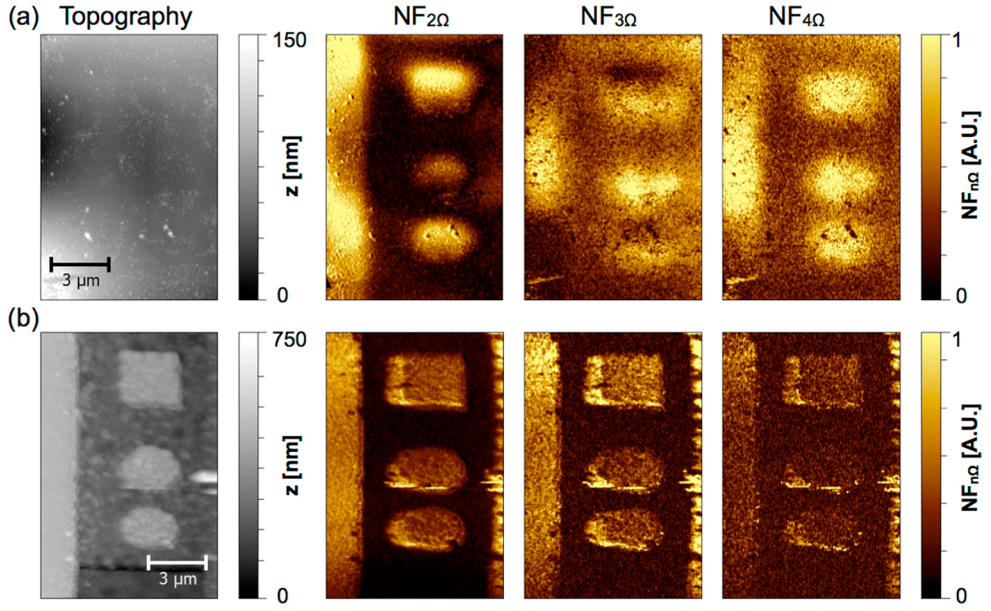

Figure 3. Near-field images of superlensed signal (a) and reference objects (b). (a) Scans of the BTO lamella show (from left to right) the sample topography and the near-field signals $NF_{n\Omega}$ at λ = 16.5 μm demodulated at different higher harmonics 2Ω, 3Ω, and 4Ω. (b) Corresponding scans on the reference objects imaged at the same conditions. Note that the total size of the lamella in all three spatial dimensions is smaller than the wavelength, while the image resolution is clearly below 1 μm. Scan data in (a) and (b) are shown in the same color scales for the same harmonic signals and, hence, are directly comparable.

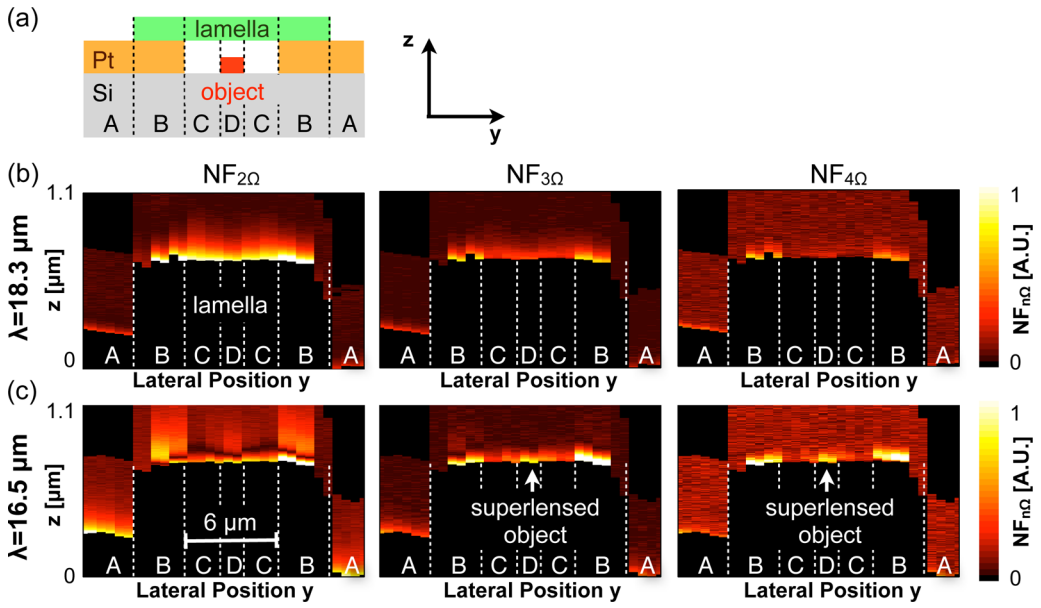

Figure 4. Near-field z–y cross sections. All images show near-field data displayed in color scales as a function of distance z (signal recording up to Δz = 500 nm from the surface) and lateral position y on the sample. (a) Sketch of the sample structure matching the y-scale of the cross sections. Areas (A) are located on the surface of the platinized substrate, whereas (B)–(D) are positions on the lamella with (B) Pt film, (C) Si substrate, and (D) Pt object on the opposite side of the lens. (b, c) From left to right, near-field signals are demodulated at increasing higher harmonic frequencies $n\Omega$ displayed in the same color scales for the same harmonic signals. (b) At λ = 18.3 μm, the excitation of a nonlocalized polariton mode results in a bright near-field response evanescently decaying anywhere at the BTO lamella surface [areas (B)–(D)]. (c) At the superlensing wavelength (λ = 16.5 μm), the object structure becomes visible in the center of the lamella (D).

objects appear uniformly bright, as they are illuminated indirectly via the near-field probe. Moreover, the superlens transfers the near-field information on the objects to the image plane at a distance of about 500 nm from the objects, whereas without the lens, this signal typically decays to zero within a distance of z = 200 nm (see Supporting Information, Figure S2).

Near-Field Cross Sections and Spectral Response. In order to study the z-decay of the near-field signals (i.e., the signal decay perpendicular to the sample surface), we record cross sections at several wavelengths along a line section of the lamella (see Figure 1d). In Figure 4, we focus on the two cases of off-resonant (Figure 4b) and on-resonant (Figure 4c) superlens excitation; full data sets as well as corresponding

DOI: 10.1021/acsphotonics.5b00365
ACS Photonics 2016, 3, 20–26

measurements on the reference structure are available in the Supporting Information (see Figures S2–S4). Here though, we display different harmonics $NF_{n\Omega}$ showing reduced far-field contributions with increasing n (note that the same color scales are used for the same harmonics, while the scales of different harmonics are not comparable).

Figure 4b displays the excitation with λ = 18.3 μm for which a bright near-field signal close to the Pt surface (areas (A)) as well as on the lamella (areas (B)–(D), elevated area in the center) can be observed. Here, particularly at higher harmonics, the areas at which the Pt edge and lamella overlap (areas (B)) appear brightest. However, even though a polariton mode in BTO enhances the near-field signal resonantly, the object structure in the center (area (D)) is not reconstructed, as the superlensing condition is not met.

On the other hand, at the superlensing wavelength around λ = 16.5 μm (Figure 4c), the object contours become clearly discernible in the center of the lamella (area (D)). Here, the higher the harmonic order the more distinct is the confinement of the structure. Note that the second harmonic near-field signal may still include some spurious contribution from the optical far field reaching a nonzero value even at larger distances z between tip and sample surface (see Figure 4c, $NF_{2\Omega}$). However, all the higher harmonics $n\Omega$ with n > 2 display pure near-field signatures with the electric field evanescently bound to all the sample surfaces, that is, on the Pt film, the lamella and the superlensing areas.

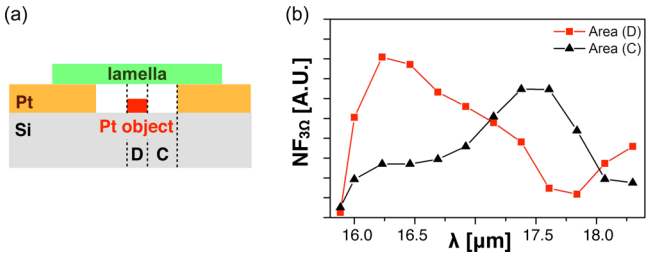

Figure 5. Near-field spectra of the lamella superlens. (a) Sample structure showing the areas (C) and (D) where the spectra in (b) were recorded. (b) The characteristic spectra show two modes in the sample, namely, top-layer polariton excitation at around λ = 17.5 μm, which dominates on area (C), and the two-interface-polariton coupling peaking at λ = 16.3 μm for superlensing an area (D). Note that it is the latter mode only that forms the superlensing effect and, consequently, results in subdiffraction-limited resolution.

From the recorded cross sections, we extract the spectral signatures of the superlens (area (D)) and compare them to the response of the lamella without superlensed objects (area (C), see Figure 5). The lamella itself (area (C)) shows an enhanced near-field response[8,9] for λ = 16–18 μm whenever the real part of its permittivity lies between −5 and −1. For a zero tip–sample distance, we observe a clear peak at λ = 17.5 μm, as well as a shoulder at λ = 16.3 μm. On the other hand, the superlensed signal (area (D)) shows a maximum at λ = 16.3 μm, where the superlensing condition is met. This characteristic response was already reported in ref 16 and illustrates the presence of two modes in the sample, namely the top-layer polariton excitation and a two-interface-polariton coupling. Note that the latter is responsible for the superlensing effect and consequently results in the desired subdiffraction-limited resolution.

All experimental findings are in excellent agreement with our theoretical predictions. The largest superlensed signal strength (Figure 5) occurs at λ = 16.3 μm and highest lateral resolution (Figures 3 and 4) has been observed at λ = 16.5 μm corresponding exactly to the transfer of highest $\mathbf{k}_x$-components (see Figure 2). Note that by using other lamella materials, the concept of the local superlens can be applied to any wavelength regime of interest. In fact, as the bandwidth of superlensing is naturally narrow due to its resonant character (for BTO about $\Delta\lambda$ = 1 μm at λ = 16.3 μm), it is the specimen of interest that will determine the wavelength and with that the material to choose for the lens. Bottlenecks of the proposed design include material absorption and interface roughness, which both decrease the resolution of the superlens. Moreover, the lens is read out by local SNOM-scanning, which limits the speed of detection. However, compared to direct measurements, the examination via SNOM clearly has been facilitated in terms of signal enhancement and scanning by the usage of the local superlens. In general, the proposed method is not limited in its application to trenches or channels, as examined here; however, when superlenses with much smaller lateral dimensions are required, one needs to take alterations of the image due to the finite size into account (see Supporting Information, Figure S1).

CONCLUSIONS

In summary, this work presents near-field investigations on a local superlens that consists of a single dielectric BTO lamella. In agreement with theory, we observe superlens imaging beyond the diffraction limit with an enhanced signal strength compared to the reference structure. The lens itself has a size much smaller than the superlensing wavelength, unambiguously demonstrating the localized character of the underlying coupled polariton modes. More explicitly, the superlensing layer does not need to be extended in the two-dimensional plane, since sufficient $\mathbf{k}$-vectors contribute to the superlensed image reconstruction even for a limited active superlens area. The small dimensions of this lens allow one to controllably place it on areas of interest without the need of large-scale growth or lithography. Moreover, as the lens surface is topographically flat, scanning-probe microscopy based imaging is facilitated especially for objects exhibiting a larger topography or for hard-to-scan environments such as, for example, liquids. Compared to earlier perovskite-based lenses, the lamella superlens may be engineered above any desired object without facing limitations, clearly favoring elegant applications in complex structures such as lab-on-chip environments. Hence, we envision application of subwavelength-sized lamella superlenses as “near-field windows” into waveguides or flow cells for remote sensing.

METHODS

Fabrication of the Lamella Superlens. The lamella superlens introduced here consists of a planar slab of single crystalline BTO balancing across the objects of interest that are located within a ~0.3 μm deep trench in a platinized silicon substrate (Figure 1a). The trench structure was fabricated by selective ion-beam etching using a FEI Nova 600 DualBeam model FIB microscope, such that two sets of subwavelength sized platinum (Pt) objects remained in the gap (each consisting of a 2 μm × 2 μm square and two 2 μm diameter circles with a height of ~200 nm). A $(100)_{pc}$-faced lamella measuring 13.5 μm × 10.5 μm × 400 nm was machined from a

DOI: 10.1021/acsphotonics.5b00365
ACS Photonics 2016, 3, 20–26

commercially obtained bulk BTO single crystal using a FIB milling approach.[30] The lamella was then cut free from the bulk and placed across the milled trench on the substrate using a micromanipulator-controlled fine-tipped glass needle. According to a previously established methodology, the lamella was annealed for 60 min at 700 °C to recrystallize ion-beam induced surface damage[31] and etched with 3 M hydrochloric acid for 5 min to remove gallium contaminants expelled to the surface.[32] Although measuring only a few 100 nm in thickness, such lamellae are known to behave almost completely like bulk and do not suffer the degradation in properties seen in conventional thin films.[29,33]

Scattering Scanning Near-Field Optical Microscopy in Combination with a Free-Electron Laser. We combine scattering scanning near-field optical microscopy (s-SNOM) with the tunable free-electron laser (FEL) FELBE at the Helmholtz-Zentrum Dresden-Rossendorf.[9,10,16,17] The narrow-band FEL is precisely tunable in the broad range from 4 to 250 μm in wavelength, hence excellently matching the needs for resonant BTO lamella excitation around λ_{SL} = 16.5 μm. The s-SNOM is based on a noncontact atomic force microscope (nc-AFM) operated at an Ω = 170 kHz cantilever resonance frequency with a 50 nm oscillation amplitude.[9,10,16,17] The ∼20 mW p-polarized FEL radiation illuminates the SNOM-probe at an incident angle of 65° with respect to the sample normal (see Figure 1d), while the scattered light is detected in back-scattering direction using a photoconductive mercury–cadmium–telluride (MCT) detector.

■ ASSOCIATED CONTENT

Supporting Information

The Supporting Information is available free of charge on the ACS Publications website at DOI: 10.1021/acsphotonics.5b00365.

Theoretical considerations concerning the role of lateral superlens' size (Figure S1). Near-field cross sections on the reference structure at wavelengths corresponding to on- and off-resonant excitation of the BTO superlens (Figure S2). Near-field cross sections on both, the lamella superlens (Figure S3) and the reference dots (Figure S4), for various wavelengths between 15.7 and 18.3 μm and different harmonic demodulation at 2Ω, 3Ω, and 4Ω (PDF).

■ AUTHOR INFORMATION

Corresponding Author

*E-mail: susanne.kehr@iapp.de. Phone: +49 351 463 32711. Fax: +49 351 463 37065.

Notes

The authors declare no competing financial interest.

■ ACKNOWLEDGMENTS

The authors thank both the FELBE team of HZDR and Markus Fehrenbacher for dedicated support. J.M.G. and R.G.P.M. acknowledge financial support from the Engineering and Physical Sciences Research Council (EPSRC) under Grant Number EP/J017191/1. S.C.K., L.O., T.K., J.D., F.K., D.L., and L.M.E. acknowledge the support by the German Science Foundation (DFG) through the Cluster of Excellence "Center for Advancing Electronics Dresden" and under Grad Number KE2068/2-1 as well as funding by the BMBF Grant 05K10ODB. L.O. holds a scholarship of the *Studienstiftung des Deutschen Volkes*.

■ REFERENCES

(1) Betzig, E.; Patterson, G. H.; Sougrat, R.; Lindwasser, O. W.; Olenych, S.; Bonifacino, J. S.; Davidson, M. W.; Lippincott-Schwartz, J.; Hess, H. F. Imaging Intracellular Fluorescent Proteins at Nanometer Resolution. *Science* **2006**, *313*, 1642–1645.

(2) Klar, T. A.; Jakobs, S.; Dyba, M.; Egner, A.; Hell, S. W. Fluorescence microscopy with diffraction resolution barrier broken by stimulated emission. *Proc. Natl. Acad. Sci. U. S. A.* **2000**, *97*, 8206–8210.

(3) Dickson, R. M.; Cubitt, A. B.; Tsien, R. Y.; Moerner, W. E. On/off blinking and switching behaviour of single molecules of green fluorescent protein. *Nature* **1997**, *388*, 355–358.

(4) Ash, E. A.; Nicholls, G. Super-resolution aperture scanning microscope. *Nature* **1972**, *237*, 510–512.

(5) Betzig, E.; Trautman, J. K. Near-field optics: microscopy, spectroscopy, and surface modification beyond the diffraction limit. *Science* **1992**, *257*, 189–195.

(6) Brehm, M.; Taubner, T.; Hillenbrand, R.; Keilmann, F. Infrared spectroscopic mapping of single nanoparticles and viruses at nanoscale resolution. *Nano Lett.* **2006**, *6*, 1307–1310.

(7) Huth, F.; Govyadinov, A.; Amarie, S.; Nuansing, W.; Keilmann, F.; Hillenbrand, R. Nano- FTIR Absorption Spectroscopy of Molecular Fingerprints at 20 nm Spatial Resolution. *Nano Lett.* **2012**, *12*, 3973–3978.

(8) Hillenbrand, R.; Taubner, T.; Keilmann, F. Phonon-enhanced light–matter interaction at the nanometre scale. *Nature* **2002**, *418*, 159–162.

(9) Kehr, S. C.; Cebula, M.; Mieth, O.; Härtling, T.; Seidel, J.; Grafström, S.; Eng, L. M.; Winnerl, S.; Stehr, D.; Helm, M. Anisotropy Contrast in Phonon-Enhanced Apertureless Near-Field Microscopy Using a Free-Electron Laser. *Phys. Rev. Lett.* **2008**, *100*, 256403.

(10) Döring, J.; von Ribbeck, H.-G.; Fehrenbacher, M.; Kehr, S. C.; Eng, L. M. Near-field resonance shifts of ferroelectric barium titanate domains upon low-temperature phase transition. *Appl. Phys. Lett.* **2014**, *105*, 053109.

(11) Jacob, R.; Winnerl, S.; Fehrenbacher, M.; Bhattacharyya, J.; Schneider, H.; Wenzel, M. T.; von Ribbeck, H.-G.; Eng, L. M.; Atkinson, P.; Schmidt, O. G.; Helm, M. Intersublevel Spectroscopy on Single InAs-Quantum Dots by Terahertz Near-Field Microscopy. *Nano Lett.* **2012**, *12*, 4336–4340.

(12) Koenderink, A. F.; Alù, A.; Polman, A. Nanophotonics: shrinking light-based technology. *Science* **2015**, *348*, 516–521.

(13) Pendry, J. B. Negative refraction makes a perfect lens. *Phys. Rev. Lett.* **2000**, *85*, 3966–3969.

(14) Korobkin, D.; Urzhumov, Y.; Shvets, G. Enhanced near-field resolution in midinfrared using metamaterials. *J. Opt. Soc. Am. B* **2006**, *23*, 468–478.

(15) Taubner, T.; Korobkin, D.; Urzhumov, Y.; Shvets, G.; Hillenbrand, R. Near-field microscopy through a SiC superlens. *Science* **2006**, *313*, 1595.

(16) Kehr, S. C.; Liu, Y. M.; Martin, L. W.; Yu, P.; Gajek, M.; Yang, S.- Y.; Yang, C.-H.; Wenzel, M. T.; Jacob, R.; von Ribbeck, H.-G.; Helm, M.; Zhang, X.; Eng, L. M.; Ramesh, R. Near-Field Examination of Perovskite-Based Superlenses and Superlens-Enhanced Probe-Object Coupling. *Nat. Commun.* **2011**, *2*, 249.

(17) Kehr, S. C.; Yu, P.; Liu, Y. M.; Parzefall, M.; Khan, A. I.; Jacob, R.; Wenzel, M. T.; von Ribbeck, H.-G.; Helm, M.; Zhang, X.; Eng, L. M.; Ramesh, R. Microspectroscopy on Perovskite-Based Superlenses. *Opt. Mater. Express* **2011**, *1*, 1051–1060.

(18) Fang, N.; Lee, H.; Sun, C.; Zhang, X. Sub-diffraction-limited optical imaging with a silver superlens. *Science* **2005**, *308*, 534–537.

(19) Fehrenbacher, M.; Winnerl, S.; Schneider, H.; Döring, J.; Kehr, S. C.; Eng, L. M.; Huo, Y.; Schmidt, O. G.; Yao, K.; Liu, Y.; Helm, M. Plasmonic Superlensing in Doped GaAs. *Nano Lett.* **2015**, *15*, 1057–1061.

DOI: 10.1021/acsphotonics.5b00365
ACS Photonics 2016, 3, 20–26

(20) Li, P.; Taubner, T. Broadband subwavelength imaging using a tunable graphene-lens. *ACS Nano* **2012**, *6*, 10107−10114.
(21) Li, P.; Wang, T.; Böckmann, H.; Taubner, T. Graphene-enhanced infrared near-field microscopy. *Nano Lett.* **2014**, *14*, 4400−4405.
(22) Caldwell, J. D.; Lindsay, L.; Giannini, V.; Vurgaftman, I.; Reinecke, T. L.; Maier, S. A.; Glembocki, O. J. Low-Loss, Infrared and Terahertz Nanophotonics Using Surface Phonon Polaritons. *Nanophotonics* **2015**, *4*, 44−68.
(23) McGilly, L. J.; Schilling, A.; Gregg, J. M. Domain bundle boundaries in single crystal $BaTiO_3$ lamellae: searching for naturally forming dipole flux-closure/quadrupole chains. *Nano Lett.* **2010**, *10*, 4200−4205.
(24) Aubry, A.; Pendry, J. B. Mimicking a negative refractive slab by two phase conjugators. *J. Opt. Soc. Am. B* **2010**, *27*, 72−83.
(25) Servoin, J. L.; Gervais, F.; Quittet, A.; Luspin, Y. Infrared and Raman responses in ferroelectric perovskite crystals. *Phys. Rev. B: Condens. Matter Mater. Phys.* **1980**, *21*, 2038−2041.
(26) Born, M.; Wolf, E. *Principles of Optics: Electromagnetic Theory of Propagation, Interference and Diffraction of Light*; Cambridge University Press, 1999.
(27) Solymar, L.; Shamonina, E. *Waves in Metamaterials*; Oxford University Press, 2009.
(28) Wurtz, G.; Bachelot, R.; Royer, P. A. Reflection-mode apertureless scanning near-field optical microscope developed from a commercial scanning probe microscope. *Rev. Sci. Instrum.* **1998**, *69*, 1735−1743.
(29) Knoll, B.; Keilmann, F. Enhanced dielectric contrast in scattering-type scanning near-field optical microscopy. *Opt. Commun.* **2000**, *182*, 321−328.
(30) Chang, L.-W.; McMillen, M.; Morrison, F. D.; Scott, J. F.; Gregg, J. M. Size effects on thin film ferroelectrics: experiments on isolated single crystal sheets. *Appl. Phys. Lett.* **2008**, *93*, 132904.
(31) Schilling, A.; Adams, T.; Bowman, R. M.; Gregg, J. M. Strategies for gallium removal after focused ion beam patterning of ferroelectric oxide nanostructures. *Nanotechnology* **2007**, *18*, 035301.
(32) McGilly, L. J.; Gregg, J. M. Scaling of superdomain bands in ferroelectric dots. *Appl. Phys. Lett.* **2011**, *98*, 132902.
(33) Chang, L.-W.; Alexe, M.; Scott, J. F.; Gregg, J. M. Settling the ″dead layer″ debate in nanoscale capacitors. *Adv. Mater.* **2009**, *21*, 4911−4914.

DOI: 10.1021/acsphotonics.5b00365
ACS Photonics 2016, 3, 20−26